

PINN-MEP: CONTINUOUS NEURAL REPRESENTATIONS FOR MINIMUM-ENERGY PATH DISCOVERY IN MOLECULAR SYSTEMS

Magnus Petersen

Goethe University Frankfurt, Frankfurt Institute for Advanced Studies
mapetersen@fias.uni-frankfurt.de

Roberto Covino

Goethe University Frankfurt, Frankfurt Institute for Advanced Studies
covino@fias.uni-frankfurt.de

ABSTRACT

Characterizing conformational transitions in physical systems remains a fundamental challenge, as traditional sampling methods struggle with the high-dimensional nature of molecular systems and high energy barriers between stable states. These rare events often represent the most biologically significant processes, like ion channel opening that controls cellular signaling, yet may require months of continuous simulation to observe. We present a method that reformulates transition path generation as a continuous optimization problem solved through physics-informed neural networks (PINNs) inspired by string methods for minimum-energy path (MEP) generation. By representing paths as implicit neural functions and leveraging automatic differentiation with differentiable molecular force fields, our method efficiently discovers physically realistic transition pathways without expensive sampling. We demonstrate our approach on two proteins, including an explicitly hydrated BPTI system with more than 8,300 atoms. Our method identifies a representative minimum-energy path for the conformational change captured in a millisecond-scale MD simulation (Shaw et al., 2010), while requiring only $\sim 480,000$ force field evaluations compared to approximately 412 billion in the original study. Though our method yields a single pathway rather than an ensemble of transition trajectories, this represents a six orders of magnitude reduction in computational cost, generating a physically meaningful transition in less than 15 minutes on a standard GPU rather than weeks on specialized hardware.

1 INTRODUCTION

Characterizing molecular conformational changes, or transitions, is essential for understanding biological processes, from enzyme catalysis to protein folding. Although molecular dynamics (MD) simulations provide unprecedented atomic-level detail of these processes (Dror et al., 2012), capturing rare transition events remains computationally challenging due to the inherent timescale gap between molecular motion and conformational changes. This difficulty arises from transition rates between stable states being exponentially suppressed by the height of the energy barriers that separate them, as described by transition state theory (Eyring, 1935). As a result, direct simulation methods spend the vast majority of computational effort sampling already known stable states, making the observation of transitions between them prohibitively expensive.

The search for efficient methods to identify transition pathways between stable states has a rich history in computational physics. Early theoretical work established key principles through the Freidlin-Wentzell (Freidlin & Wentzell, 1998) and Onsager-Machlup (Onsager & Machlup, 1953) functionals, which connect the most probable trajectories, including transitions, to minimizers of specific action functionals. Building on these foundations, the minimum-energy path (MEP) between stable molecular states represents the most probable transition pathway in the limit of high

friction. This path reveals the mechanism of conformational change, identifies key transition states and intermediate configurations, and can thus be highly informative about the system’s dynamics. Moreover, the MEP can serve as a scaffold for subsequent sampling of the full transition path ensemble, making it a powerful tool for understanding molecular dynamics. Methods such as the string method family or chain-of-states approaches (E et al., 2002; 2005; Ren et al., 2005; Maragliano et al., 2006; E et al., 2007; Petersen et al., 2024; Dellago et al., 1998) approximate these paths as splines or as a discrete series of molecular configurations connected by artificial spring forces to ensure continuity. Despite their strong theoretical foundation, these approaches face fundamental challenges stemming from their optimization in Cartesian molecular coordinates. The discrete chain of conformations requires periodic reparameterization to maintain even spacing, leading to a complex alternation between energy minimization and geometric constraints. Additional limitations include the difficulty of generating good initial transition guesses and limited parallelization, which restricts the scale of practical applications. While this formulation has proven useful for small-scale systems, it has not yet benefited from modern optimization approaches that could address these challenges.

Recent advances in machine learning methodology have created opportunities for novel approaches to this challenge. Physics-informed neural networks (PINNs) have increased our ability to solve complex physical problems by embedding differential equations directly into neural architectures (Raissi et al., 2019). Additionally, the development of differentiable molecular force fields (Wang et al., 2023) has enabled seamless integration of physical force field models used in MD simulations with modern machine learning frameworks, allowing efficient computation of derivatives beyond forces, which are needed for neural path optimization.

Numerous approaches have emerged over the past decades to tackle the problem of sampling transitions. Traditional simulation-based sampling methods (Jung et al., 2023; Lazzeri et al., 2023; Bolhuis et al., 2002; Dellago et al., 1998; Laio & Parrinello, 2002; Torrie & Valleau, 1977) rely on expensive molecular dynamics simulations, often requiring initial MD-harvested transition trajectories or prior knowledge of the transition dynamics to begin with. More recent machine learning approaches have explored several directions: variational approaches using Doob’s h-transform (Du et al., 2024; Lee et al., 2025; Das & Limmer, 2019; Singh & Limmer, 2023), stochastic control formulations (Yan et al., 2022; Holdijk et al., 2023), and even attempts to sample transition trajectories directly using diffusion models (Petersen et al., 2023; Han et al., 2024; Jing et al., 2024).

Notably, Du et al. (2024) uses a similar neural representation of transition paths but with a different objective, targeting the complete transition path ensemble by additionally parameterizing path width and optimizing based on a framework rooted in Doob’s h-transform (Doob, 1957) and Wasserstein Lagrangian flows (Neklyudov et al., 2024). Most closely related to our method, Ramakrishnan et al. (2025) employ a continuous neural parameterization of MEPs inspired by Nudged Elastic Band (NEB) methods, a class of methods related to string methods, incorporating specialized components for tangential forces, path velocity, and transition state energetics to optimize the neural path. Another promising concurrent approach by Raja et al. (2025) creatively leverages pretrained diffusion models as a sampler of initial transition conformations and as a force field to generate plausible transition paths using the discretized Onsager-Machlup action directly as a loss function. While each approach offers valuable insights into neural network-based path discovery, our method focuses on a streamlined optimization scheme that efficiently scales to much larger biomolecular systems with explicit solvent, essential for accurately modeling such systems, while maintaining fast training times.

Drawing inspiration from neural implicit representations in computer vision (Mildenhall et al., 2020; Sitzmann et al., 2020), we reformulate the traditional minimum-energy-path finding problem as a continuous optimization framework. Our approach transforms the Onsager-Machlup functional, which naturally models the probability of paths in stochastic systems, into a remarkably simple and intuitive loss function that requires only energy evaluations along the neural network parametrized path. In contrast to existing methods that use complex composite losses involving energies, forces, and path gradients, our streamlined formulation eliminates the need for these additional computations. This simplification, while faster, also sidesteps known issues in PINN optimization if the loss contains differential operators (Rathore et al., 2024). This PINN framework efficiently captures physically meaningful transition mechanisms for complex biomolecular systems, completing optimization in minutes on standard hardware.

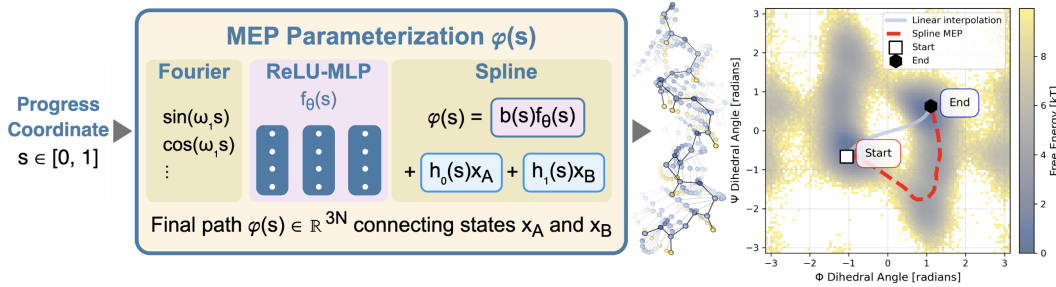


Figure 1: Overview of the PINN-MEP neural architecture and results on our 129-atom AIB9 toy system. **Left:** The neural parameterization of MEPs transforms a progress coordinate $s \in [0, 1]$ into molecular configurations through a combination of sinusoidal/Fourier embeddings, neural network processing, and smooth boundary handling with basis functions. The final path $\phi(s) \in \mathbb{R}^{3N}$ continuously connects start and end states x_A and x_B . A visualization of the molecular conformational changes is shown alongside, with the opacity determined by the progress coordinate. **Right:** Projection of the discovered transition path onto the ϕ - ψ dihedral angle space of the central amino acids for the AIB9 system, overlaid on the free energy landscape determined by a long MD simulation. The neural network path (red, dashed) naturally discovers physically realistic routes through low-energy valleys, while direct linear interpolation (blue, solid) crosses high-energy barriers, demonstrating the method’s ability to find meaningful transition mechanisms.

2 THEORY AND METHODS

2.1 DERIVATION OF THE ENERGY-BASED LOSS FUNCTION AND NEURAL IMPLEMENTATION

To derive our loss function, which when minimized yields a continuous curve representing the MEP connecting fixed endpoints x_A and x_B , we build upon alternative formulations of the Onsager-Machlup action functional as explored by Vandend-Eijnden & Heymann (2008) and Olander & Elber (1997) in the context of string methods. However, we further simplify the approach after reaching their geometric formulation. A complete derivation with all mathematical details is provided in Appendix A.1. We begin with a molecular system evolving under overdamped Langevin dynamics, a model for molecular motion in the high-friction regime characteristic of biomolecular systems:

$$\dot{x}(t) = -\nabla U(x(t)) + \sqrt{2}\eta(t) \quad (1)$$

$U(x)$ represents the potential energy function, $\eta(t)$ is Gaussian white noise modeling thermal fluctuations, and physical constants are absorbed into the nondimensionalization. To derive the path probability, we discretize the time interval $[0, T]$ into N steps of duration Δt , approximating the dynamics as:

$$x_{i+1} = x_i - \Delta t \nabla U(x_i) + \sqrt{2\Delta t} \eta_i \quad (2)$$

where η_i are independent standard Gaussian random variables. The conditional probability of transitioning from x_i to x_{i+1} follows a Gaussian distribution:

$$P(x_{i+1}|x_i) \propto \exp\left(-\frac{(x_{i+1} - x_i + \Delta t \nabla U(x_i))^2}{4\Delta t}\right) \quad (3)$$

Taking the product of these conditional probabilities over all time steps N and then taking the limit as $\Delta t \rightarrow 0$ yields the path probability:

$$\mathbb{P}[x(t)] \propto \exp\left(-\frac{1}{4} \int_0^T \|\dot{x}(t) + \nabla U(x(t))\|^2 dt\right) \quad (4)$$

The exponent corresponds to the Onsager-Machlup action functional Onsager & Machlup (1953):

$$S_{\text{OM}}[x] = \frac{1}{4} \int_0^T \|\dot{x}(t) + \nabla U(x(t))\|^2 dt \quad (5)$$

Thus, maximizing the probability of a transition path (subject to fixed endpoints $x(0) = x_A$ and $x(T) = x_B$) is equivalent to minimizing this action functional. Notably, there are different derivations of the action that yield an additional higher-order derivative term related to trajectory entropy, whose necessity is conditional on the task (Adib, 2008). Since we are primarily interested in MEPs, we neglect this term. However, the resultant MEPs still empirically align well with the free energy landscape. To further simplify, we expand the integrand of the action functional:

$$\left\| \dot{x}(t) + \nabla U(x(t)) \right\|^2 = \|\dot{x}(t)\|^2 + 2\dot{x}(t) \cdot \nabla U(x(t)) + \|\nabla U(x(t))\|^2 \quad (6)$$

For paths with fixed endpoints, the cross-term integrates to a constant difference in potential energy:

$$\int_0^T \dot{x}(t) \cdot \nabla U(x(t)) dt = U(x_B) - U(x_A) \quad (7)$$

Since x_A and x_B are fixed in our formulation, this term becomes a constant that doesn't affect the optimization. We can therefore focus on minimizing the remaining terms. Applying the Cauchy-Schwarz inequality to the remaining terms:

$$\|\dot{x}(t)\|^2 + \|\nabla U(x(t))\|^2 \geq 2\|\dot{x}(t)\|\|\nabla U(x(t))\| \quad (8)$$

This upper bound becomes an equality when $\dot{x}(t)$ is parallel or antiparallel to $\nabla U(x(t))$, with the direction determined by whether the path is ascending or descending the energy landscape. Crucially, we allow the path to optimize its shape and length in our formulation. This freedom enables the path to adjust to follow the energy gradient (or its opposite), making the above upper bound tight at the optimum. When we abandon fixed-time parameterization and allow the path to stretch as needed to align with energy gradients, we can transform the time integral into a purely geometric one by defining the arc-length element $ds_{arc} = \|\dot{x}(t)\| dt$ along the spatial curve φ :

$$\int_0^T \|\nabla U(x(t))\| \|\dot{x}(t)\| dt = \int_{\varphi} \|\nabla U(x)\| ds_{arc} \quad (9)$$

While the referenced works (Vanden-Eijnden & Heymann, 2008; Olander & Elber, 1997) derive and use this geometric action, we further simplify it. This geometric integral represents a natural endpoint for theoretical development for traditional chain-of-states and string methods. In these classical approaches, forces $-\nabla U(x)$ directly update molecular conformations x to minimize $U(x)$, making minimization along a discretized string using forces conceptually straightforward.

However, we want a loss function that acts directly on the neural network parameters θ in our neural network formulation. While we could parameterize the path using a neural network and then compute forces along the path before backpropagating to our parameters, this would introduce additional gradient computations, which have been noted to lead to optimization challenges in PINNs (Rathore et al., 2024). We avoid this issue by simplifying to an energy-based loss.

We represent the transition path as a continuous neural mapping $\varphi_{\theta}(s)$ from a progress coordinate $s \in [0, 1]$ to the system's Cartesian coordinates, such that $\varphi_{\theta}(0) = x_A$ and $\varphi_{\theta}(1) = x_B$. We then discretize the path into segments:

$$\int_{\varphi} \|\nabla U(x)\| ds_{arc} \approx \sum_{k=0}^{L-2} \|\nabla U(\varphi_k)\| \|\Delta\varphi_k\| \quad (10)$$

where $\varphi_k = \varphi(s_k)$ and $\Delta\varphi_k = \varphi_{k+1} - \varphi_k$.

For a path segment, applying Taylor's theorem, we can express the energy difference as:

$$U(\varphi_{k+1}) - U(\varphi_k) = \nabla U(\varphi_k) \cdot \Delta\varphi_k + O(\|\Delta\varphi_k\|^2) \quad (11)$$

$$= \|\nabla U(\varphi_k)\| \|\Delta\varphi_k\| \cos \theta_k + O(\|\Delta\varphi_k\|^2) \quad (12)$$

Where θ_k is the angle between the gradient and displacement vectors. For MEPs, the displacement aligns with or against the gradient direction ($\cos \theta_k \rightarrow \pm 1$) giving:

$$\|\nabla U(\varphi_k)\| \|\Delta\varphi_k\| \approx |U(\varphi_{k+1}) - U(\varphi_k)| \quad (13)$$

This gives us a surrogate objective with the same minimum:

$$\sum_{k=0}^{L-2} \|\nabla U(\varphi_k)\| \|\Delta \varphi_k\| \approx \sum_{k=0}^{L-2} |U(\varphi_{k+1}) - U(\varphi_k)| \quad (14)$$

Using the triangle inequality on the absolute energy differences, we can establish that minimizing the simple sum of energies along the path provides an upper bound on this action:

$$\sum_{k=0}^{L-2} |U(\varphi_{k+1}) - U(\varphi_k)| \leq \sum_{k=0}^{L-1} U(\varphi_k) - (L-1) \min_k U(\varphi_k) - \frac{U(\varphi_0) + U(\varphi_{L-1})}{2} \quad (15)$$

Where $\min_k U(\varphi_k)$ is the lowest energy along the path. Since the latter terms are constants during optimization, this leads to our final loss function. To implement this in practice, we sample B points along a parametrized path $\varphi_\theta(s)$ and directly minimize the sum of energies at these points, yielding:

$$\mathcal{L}(\theta) = \frac{1}{B} \sum_{j=1}^B U(\varphi_\theta(s_j)) \quad (16)$$

where s_j are uniformly or randomly sampled points in $[0, 1]$. By minimizing $\mathcal{L}(\theta)$, we drive the path representation to discover low-energy regions connecting stable states, approximating the MEP predicted by the Onsager-Machlup framework.

2.1.1 NEURAL REPRESENTATION OF MEPs

We propose representing the path $\varphi_\theta(s)$ using a neural parameterization, similar to the mean parameterization of Du et al. (Du et al., 2024). While our approaches share similar representations, they differ in objectives and computational efficiency (see Appendix B.1 for theoretical connections and performance comparisons, respectively). Specifically, we construct a continuous function mapping a progress coordinate $s \in [0, 1]$ to molecular configurations $\varphi_\theta(s) \in \mathbb{R}^{3N}$, where N is the number of atoms, as illustrated in Figure 1 (left):

$$\varphi_\theta(s) = h_0(s)x_A + h_1(s)x_B + b(s)f_\theta(s) \quad (17)$$

Here f_θ is a neural network, $h_0(s)$ and $h_1(s)$ are basis functions that satisfy the endpoint constraints $h_0(0) = 1$, $h_0(1) = 0$, $h_1(0) = 0$, and $h_1(1) = 1$, ensuring that $\varphi_\theta(0) = x_A$ and $\varphi_\theta(1) = x_B$ regardless of the neural network’s output. While simple linear functions $h_0(s) = (1 - s)$ and $h_1(s) = s$ can be used, other basis functions with appropriate boundary conditions are also effective. The blending function $b(s)$ controls the neural network’s contribution along the path, typically designed to allow maximum influence in the transition region while smoothly vanishing at endpoints (e.g., $b(s) = s(1 - s)$).

2.1.2 PATH OPTIMIZATION

We minimize $\mathcal{L}(\theta)$ using the Adam optimizer (Kingma & Ba, 2017):

Algorithm 1 Neural MEP Optimization

- 1: **Initialize:** Parameters θ , endpoint configurations $x_A, x_B \in \mathbb{R}^{3N}$, basis functions $h_0(s), h_1(s)$ and blending function $b(s)$, learning rate α , batch size B
- 2: **Define:** Neural network $f_\theta(\cdot)$ and potential energy function $U(\cdot)$
- 3: **while** not converged **do**
- 4: Sample batch $\{s_j\}_{j=1}^B \sim \mathcal{U}[0, 1]$
- 5: $\varphi_\theta(s_j) = h_0(s_j)x_A + h_1(s_j)x_B + b(s_j)f_\theta(s_j)$
- 6: $\mathcal{L}(\theta) = \frac{1}{B} \sum_{j=1}^B U(\varphi_\theta(s_j))$
- 7: $\theta \leftarrow \text{Adam}(\alpha, \nabla_\theta \mathcal{L}(\theta))$
- 8: **end while**
- 9: **return** $\varphi_\theta(s) = h_0(s)x_A + h_1(s)x_B + b(s)f_\theta(s)$

Unlike traditional chain-of-states methods, explicit spring-like continuity terms are unnecessary; the inherent continuity of $f_\theta(s)$, combined with smooth blending functions, ensures path continuity.

2.2 ESTABLISHED APPROACHES TO MEP FINDING

Classical approaches to MEP discovery operate directly in Cartesian atomic coordinates, predating differentiable molecular force fields (Wang et al., 2023) that enable our neural network representation. This direct optimization faces significant challenges as steric clashes create extreme energy barriers that are difficult to overcome with local optimization. The string method and chain-of-states approaches discussed below represent broad families with numerous variations, extensively cataloged in reviews such as by E & Vanden-Eijnden (2010). These established techniques illustrate both foundational concepts and limitations that our approach addresses.

2.2.1 STRING METHOD

The string method (E et al., 2002; 2005; Ren et al., 2005; Maragliano et al., 2006; E et al., 2007) determines the MEPs by evolving a curve in the configuration space according to the physical forces while maintaining proper parameterization. Given the same endpoints x_A and x_B used in our formulation, the method seeks a curve (string) $\varphi(s)$ parameterized using splines mapping $s \in [0, 1]$ to the systems Cartesian coordinates that connects these states. The MEP satisfies:

$$[\nabla U]^\perp = 0 \quad (18)$$

where $[\nabla U]^\perp = \nabla U - (\nabla U \cdot \hat{\tau})\hat{\tau}$ is the component of the force perpendicular to the unit tangent vector $\hat{\tau} = \varphi'/|\varphi'|$ along the string. This orthogonality condition has an intuitive interpretation: at each point along the MEP, the forces acting on the system are entirely parallel to the path itself, with no perpendicular components trying to push the system away from the path. This represents a ridge or valley in the energy landscape—the system naturally follows the path without being forced sideways.

The simplest dynamics for evolving a curve toward this MEP is given by:

$$\frac{\partial \varphi}{\partial t} = -[\nabla U(\varphi)]^\perp + \lambda \hat{\tau} \quad (19)$$

Here $\lambda \hat{\tau}$ is a Lagrange multiplier term enforcing the parameterization constraint, typically equal arc-length parameterization where $|\varphi'(s)| = L$ (constant) for all s . In practice, the string $\varphi(s)$ is discretized into $N + 1$ images $\{\varphi_i\}_{i=0}^N$ and evolved through a two-step procedure that requires explicit reparameterization steps:

1. Evolution step:

$$\dot{\varphi}_i = -\nabla U(\varphi_i) \quad (20)$$

2. Reparameterization step to enforce equal spacing:

$$s_i = \frac{\sum_{j=0}^i |\varphi_{j+1} - \varphi_j|}{\sum_{j=0}^{N-1} |\varphi_{j+1} - \varphi_j|} \quad (21)$$

This two-step procedure converges to a discretized MEP satisfying each image's local orthogonality condition $[\nabla U]^\perp = 0$.

2.2.2 CHAIN-OF-STATES METHODS

An alternative perspective views MEP finding as optimization of a chain-of-states (Pratt, 1986; Elber & Karplus, 1987; Ulitsky & Elber, 1990; Jónsson et al., 1998; Henkelman et al., 2000; Gillilan & Lilien, 2004; Sheppard et al., 2008). Given a sequence $\{x_0, \dots, x_N\}$ with $x_0 = x_A$ and $x_N = x_B$, the objective function is defined as:

$$E(\{x_i\}_{i=1}^{N-1}) = \sum_{i=1}^{N-1} U(x_i) + \frac{k}{2} \sum_{i=1}^N \frac{|x_i - x_{i-1}|^2}{\Delta s^2} \quad (22)$$

where $\Delta s = 1/N$ and k is a spring constant. The spring term enforces the continuity of the path while allowing flexibility in the discretization. However, this formulation introduces a well-known limitation: the spring forces tend to cause "corner cutting," where the path takes shortcuts through high-energy regions rather than following the low-energy valleys representing physically meaningful transitions. Although variants of chain-of-states methods exist that avoid this limitation, they come at an increased computational cost.

3 EXPERIMENTS

We evaluate our method on two molecular systems: the AIB9 peptide and Bovine Pancreatic Trypsin Inhibitor (BPTI). These systems represent different scales of complexity and serve to validate our method's ability to discover physically meaningful transition paths. In Appendix A.2, we compare and benchmark our method with the related approaches outlined in (Du et al., 2024; Lee et al., 2025). In Appendix B.1, we present ablation studies analyzing the impact of different embedding strategies, interpolation methods, neural network architectures, and regularization approaches.

3.1 AIB9 TRANSITION PATH DISCOVERY

We first examine the AIB9 system, a 9-residue artificial protein with 129 atoms that exhibits two well-defined metastable states, making it an ideal test case for transition path methods. This system effectively bridges abstract models and complex proteins: it is small enough for extensive reference simulations yet complex enough to exhibit realistic conformational changes; its energy landscape is well-characterized; and its transitions are easily visualized through dihedral angle projections. Unlike artificial toy problems, AIB9 allows direct validation with actual biomolecular force fields. We use the AMBER ff15ipq-m force field for protein mimetics (Bogetti et al., 2020) implemented in DMFF (Wang et al., 2023), and we generate multiple MEPs between the system's two metastable states.

Figure 2 shows the discovered transition paths projected onto the central residue's ϕ - ψ dihedral angle space. The method identifies multiple physically plausible pathways between the states, which are also observed with long MD simulations. For each path, different conformations of the states were picked as start and end points; this, along with the neural network's random initialization, leads to the discovery of multiple different transitions. Notably, the discovered MEPs align well with the free energy landscape despite our choice of action functional without the trajectory entropy term and the assumption of overdamped dynamics, which may not be ideal for this vacuum system, but is less problematic for hydrated systems.

4 BPTI CONFORMATIONAL CHANGE PATHWAY

Bovine Pancreatic Trypsin Inhibitor (BPTI) is a clinically significant protein used as an anticoagulant in medical procedures. BPTI is 58 residues long (892 atoms) and has complex conformational changes involving disulfide bond rearrangements paired with backbone changes.

To investigate BPTI's conformational transitions, we use as reference structures five key states from a landmark molecular dynamics (MD) simulation performed by D.E. Shaw Research on their Anton supercomputer (Shaw et al., 2010). These publicly available snapshots provide rare benchmark structures for validating our approach to BPTI's transition mechanisms, making it an excellent larger system to test the method. Full details of our BPTI system preparation, explicit solvent shell

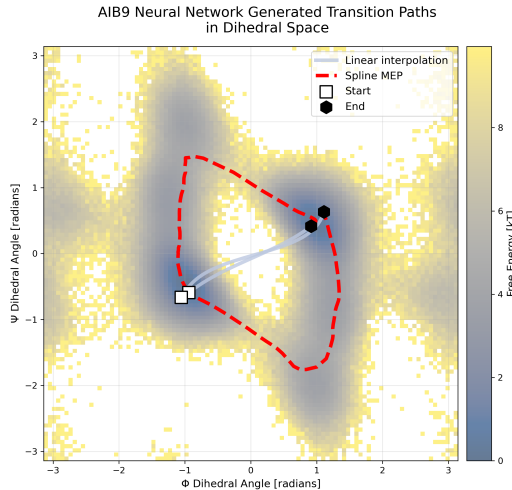


Figure 2: AIB9 free energy surface projected onto central residue dihedral angles (ϕ, ψ) . Two distinct MEPs were found with different random seeds, demonstrating the method's ability to find multiple distinct transition pathways.

construction, and hybrid neural network architecture for handling water molecules are provided in Appendix B.2.

We generate multiple transition MEPs connecting two BPTI states from the D.E. Shaw simulation. The intermediate snapshots from the D.E. Shaw simulation serve as validation points; they were not used as inputs but represent physically realized conformations from the whole trajectory. To analyze this path, we compute two collective variables matching those used in the original D.E. Shaw study: (1) the disulfide torsion angle between Cys14 and Cys38, calculated using the dihedral angle formed by CB14–SG14–SG38–CB38 atoms, and (2) the backbone RMSD, root mean square displacement, of residues 4–54 after mean-centering. Remarkably, as shown in Figure 3, our optimized path passes through all intermediate snapshots, indicating that it successfully discovers the same transition mechanism as the computationally intensive MD simulation.

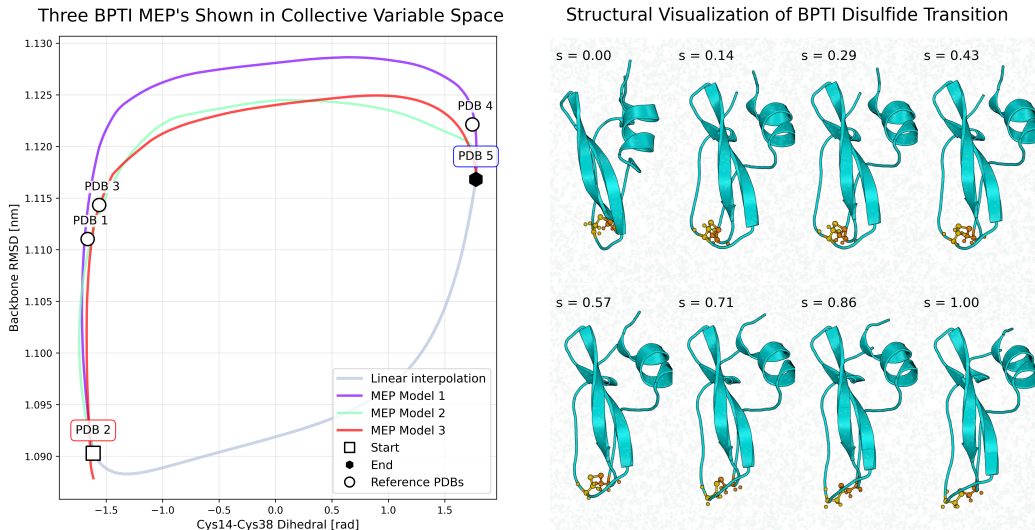


Figure 3: Analysis of our discovered BPTI transition pathway. **Left:** Evolution of BPTI dynamics projected onto two collective variables matching the original D.E. Shaw study: the Cys14–Cys38 disulfide torsion angle (formed by CB14–SG14–SG38–CB38 atoms) versus the mean-centered backbone RMSD of residues 4–54. Reference structures from the D.E. Shaw simulation are marked with circles. Our optimized paths pass through all intermediate snapshots, demonstrating that it discovers the same transition mechanism observed in the millisecond-scale MD simulation. **Right:** Structural visualization of the 8,300-atom BPTI and water system highlighting the Cys14–Cys38 disulfide bond conformation along one of our optimized transition paths. Each panel represents a different value of the progress coordinate s , showing how the disulfide bond rotates during the transition. This rotation is a key feature of the BPTI conformational change. For clarity, the protein is shown using its secondary structure representation except for the disulfide bond, and the water molecules are rendered nearly transparent.

We matched their simulation conditions by incorporating explicit water molecules in our model to ensure a meaningful comparison with the Anton simulation. We generated water shells extending 14 Å from any protein atom for both the initial and final BPTI conformations. This increases the number of atoms from 892 to 8,300. To handle water molecules during transitions, we pair proximal water molecules between start and end states using the Hungarian algorithm (Kuhn, 1955). We then model their movement using simple parameterized splines, rather than directly incorporating all water coordinates into the neural network. This hybrid neural-spline approach allows us to include explicit solvent effects while keeping computational costs low. The specific details of our water shell construction and matching algorithm are described in Appendix B.2.

The system was modeled using the AMBER99sb-ILDN force field (Lindorff-Larsen et al., 2010) with the TIP3P water model (Jorgensen et al., 1983; Neria et al., 1996). Each MEP was computed in approximately 15 minutes on a single A6000 GPU, requiring only $\sim 480,000$ force field evaluations compared to the D.E. Shaw simulation, which conducted approximately 412 billion force field

evaluations to generate the 1.03 millisecond trajectory capturing the same conformational changes. This represents a six orders of magnitude reduction in computational effort.

While our approach does not provide the same statistical ensemble information as equilibrium MD, it efficiently captures the key transition pathway, which is often the primary mechanistic insight sought by MD practitioners. For most scientifically interesting systems—typically large biomolecular complexes—equilibrium sampling of the complete conformational space or transition path ensemble remains computationally prohibitive, making identification of dominant pathways particularly valuable. It’s worth noting that even the reference millisecond-scale simulation may not have fully achieved equilibrium sampling of the conformational space. Appendix B.2.7 provides a detailed computational performance comparison.

5 LIMITATIONS

While our feedforward neural architecture can model conformational transitions, it could benefit from incorporating domain-specific structural priors to improve training efficiency and convergence speed. Furthermore, physical force fields introduce challenges through high-energy spikes that can cause training instability and divergence in some runs. Our gradient clipping approach, outlined in B.2.5, largely mitigates this issue but doesn’t universally prevent training failures.

The method has been validated primarily on small to medium-sized protein systems, and scaling to larger multi-domain proteins could require additional optimization strategies. Our approach is also constrained to systems with suitable differentiable force fields, but this limitation diminishes as more implementations become available.

Finally, while computationally efficient, our method focuses on identifying MEPs rather than sampling the full statistical ensemble of transition pathways, representing a trade-off between efficiency and exhaustively sampling a system. However, as noted in the BPTI section 4, this mechanistic insight is often a key objective for MD practitioners studying complex biomolecular transitions.

6 CONCLUSION

We demonstrated that reformulating MEP discovery as a continuous neural optimization problem enables efficient discovery of molecular transition mechanisms with unprecedented computational efficiency. Our approach transforms the complex Onsager–Machlup action functional into a straightforward energy-based loss function that eliminates the need for force and path gradient computations required by related methods, which are known to induce optimization challenges in PINNs. This work provides a practical tool for molecular dynamics practitioners that captures essential mechanistic insights without requiring specialized hardware or extensive simulation time.

While our current implementation shows promising results, several concrete directions for improvement remain. Future work should explore neural architectures that incorporate domain-specific structural priors beyond simple MLPs with sinusoidal/Fourier embeddings. Related work by Ramakrishnan et al. (2025) investigates non-uniform sampling schemes along the path that might further aid convergence for paths that constitute dramatic rearrangements. Integrating pretrained generative models suggested by Raja et al. (2025) could provide better initial transition guesses, potentially accelerating convergence by starting optimization from conformations that already respect molecular geometry. Extending the method to handle larger multi-domain proteins is also a frontier of great scientific interest, which might bring new challenges. Future work could also explore ways to estimate free energies and reaction rates from our discovered paths.

7 BROADER IMPACTS

Our research democratizes access to the study of larger molecular systems by enabling transition path studies on standard hardware. This may accelerate drug discovery and protein engineering while contributing to sustainable computing through drastically reduced energy consumption. We see no direct negative societal impacts, though we acknowledge that accelerated protein engineering capabilities could be misused in the future, and we encourage responsible use with appropriate experimental validation.

REFERENCES

Artur B. Adib. Stochastic actions for diffusive dynamics: Reweighting, sampling, and minimization. *The Journal of Physical Chemistry B*, 112(19):5910–5916, May 2008. ISSN 1520-6106, 1520-5207. doi: 10.1021/jp0751458. URL <http://arxiv.org/abs/0712.1255>. arXiv:0712.1255 [cond-mat].

Anthony T. Bogetti, Hannah E. Piston, Jeremy M. G. Leung, Chino C. Cabalteja, Darian T. Yang, Alex J. DeGrave, Karl T. Debiec, David S. Cerutti, David A. Case, W. Seth Horne, and Lillian T. Chong. A twist in the road less traveled: The AMBER ff15ipq-m force field for protein mimetics. *The Journal of Chemical Physics*, 153(6):064101, August 2020. ISSN 0021-9606. doi: 10.1063/5.0019054. URL <https://doi.org/10.1063/5.0019054>.

Peter Bolhuis, David Chandler, Christoph Dellago, and Phillip Geissler. Transition Path Sampling: Throwing Ropes over Rough Mountain Passes, in the Dark. *Annual review of physical chemistry*, 53:291–318, February 2002. doi: 10.1146/annurev.physchem.53.082301.113146.

Avishek Das and David T. Limmer. Variational control forces for enhanced sampling of nonequilibrium molecular dynamics simulations. *The Journal of Chemical Physics*, 151(24):244123, December 2019. ISSN 0021-9606, 1089-7690. doi: 10.1063/1.5128956. URL <http://arxiv.org/abs/1909.03589>. arXiv:1909.03589 [cond-mat].

Christoph Dellago, Peter G. Bolhuis, Félix S. Csajka, and David Chandler. Transition path sampling and the calculation of rate constants. *The Journal of Chemical Physics*, 108(5):1964–1977, February 1998. ISSN 0021-9606. doi: 10.1063/1.475562. URL <https://doi.org/10.1063/1.475562>.

J. L. Doob. Conditional brownian motion and the boundary limits of harmonic functions. *Bulletin de la Société Mathématique de France*, 85:431–458, 1957. ISSN 2102-622X. doi: 10.24033/bsmf.1494. URL https://www.numdam.org/item/?id=BSMF_1957__85__431_0.

Ron O. Dror, Robert M. Dirks, J.P. Grossman, Huafeng Xu, and David E. Shaw. Biomolecular Simulation: A Computational Microscope for Molecular Biology. *Annual Review of Biophysics*, 41(1):429–452, 2012. doi: 10.1146/annurev-biophys-042910-155245. URL <https://doi.org/10.1146/annurev-biophys-042910-155245>. _eprint: <https://doi.org/10.1146/annurev-biophys-042910-155245>.

Yuanqi Du, Michael Plainer, Rob Brekelmans, Chenru Duan, Frank Noé, Carla P. Gomes, Alán Aspuru-Guzik, and Kirill Neklyudov. Doob’s Lagrangian: A Sample-Efficient Variational Approach to Transition Path Sampling, December 2024. URL <http://arxiv.org/abs/2410.07974>. arXiv:2410.07974 [cs].

Weinan E and Eric Vanden-Eijnden. Transition-path theory and path-finding algorithms for the study of rare events. *Annual Review of Physical Chemistry*, 61:391–420, 2010. ISSN 1545-1593. doi: 10.1146/annurev.physchem.040808.090412.

Weinan E, Weiqing Ren, and Eric Vanden-Eijnden. String method for the study of rare events. *Physical Review B*, 66(5):052301, August 2002. doi: 10.1103/PhysRevB.66.052301. URL <https://link.aps.org/doi/10.1103/PhysRevB.66.052301>. Publisher: American Physical Society.

Weinan E, Weiqing Ren, and Eric Vanden-Eijnden. Finite Temperature String Method for the Study of Rare Events. *The Journal of Physical Chemistry B*, 109(14):6688–6693, April 2005. ISSN 1520-6106. doi: 10.1021/jp0455430. URL <https://doi.org/10.1021/jp0455430>. Publisher: American Chemical Society.

Weinan E, Weiqing Ren, and Eric Vanden-Eijnden. Simplified and improved string method for computing the minimum energy paths in barrier-crossing events. *The Journal of Chemical Physics*, 126(16):164103, April 2007. ISSN 0021-9606. doi: 10.1063/1.2720838. URL <https://doi.org/10.1063/1.2720838>.

R. Elber and M. Karplus. A method for determining reaction paths in large molecules: Application to myoglobin. *Chemical Physics Letters*, 139(5):375–380, January 1987. ISSN 0009-2614. doi: 10.1016/0009-2614(87)80576-6. URL <https://www.sciencedirect.com/science/article/pii/0009261487805766>.

Henry Eyring. The Activated Complex in Chemical Reactions. *The Journal of Chemical Physics*, 3(2):107–115, February 1935. ISSN 0021-9606. doi: 10.1063/1.1749604. URL <https://doi.org/10.1063/1.1749604>.

M. I. Freidlin and A. D. Wentzell. *Random Perturbations of Dynamical Systems*, volume 260 of *Grundlehren der mathematischen Wissenschaften*. Springer, New York, NY, 1998. ISBN 978-1-4612-6839-0 978-1-4612-0611-8. doi: 10.1007/978-1-4612-0611-8. URL <http://link.springer.com/10.1007/978-1-4612-0611-8>.

Richard E. Gillilan and Ryan H. Lilien. Optimization and dynamics of protein-protein complexes using B-splines. *Journal of Computational Chemistry*, 25(13):1630–1646, October 2004. ISSN 0192-8651. doi: 10.1002/jcc.20088.

Jiaqi Han, Minkai Xu, Aaron Lou, Haotian Ye, and Stefano Ermon. Geometric Trajectory Diffusion Models, October 2024. URL <http://arxiv.org/abs/2410.13027>. arXiv:2410.13027 [cs].

Graeme Henkelman, Blas P. Uberuaga, and Hannes Jónsson. A climbing image nudged elastic band method for finding saddle points and minimum energy paths. *The Journal of Chemical Physics*, 113(22):9901–9904, December 2000. ISSN 0021-9606. doi: 10.1063/1.1329672. URL <https://doi.org/10.1063/1.1329672>.

Lars Holdijk, Yuanqi Du, Ferry Hooft, Priyank Jaini, Bernd Ensing, and Max Welling. Stochastic Optimal Control for Collective Variable Free Sampling of Molecular Transition Paths, July 2023. URL <http://arxiv.org/abs/2207.02149>. arXiv:2207.02149 [physics, q-bio].

Bowen Jing, Hannes Stärk, Tommi Jaakkola, and Bonnie Berger. Generative Modeling of Molecular Dynamics Trajectories, September 2024. URL <http://arxiv.org/abs/2409.17808>. arXiv:2409.17808 [q-bio].

William L. Jorgensen, Jayaraman Chandrasekhar, Jeffry D. Madura, Roger W. Impey, and Michael L. Klein. Comparison of simple potential functions for simulating liquid water. *The Journal of Chemical Physics*, 79(2):926–935, July 1983. ISSN 0021-9606. doi: 10.1063/1.445869. URL <https://doi.org/10.1063/1.445869>.

Hendrik Jung, Roberto Covino, A. Arjun, Christian Leitold, Christoph Dellago, Peter G. Bolhuis, and Gerhard Hummer. Machine-guided path sampling to discover mechanisms of molecular self-organization. *Nature Computational Science*, 3(4):334–345, April 2023. ISSN 2662-8457. doi: 10.1038/s43588-023-00428-z. URL <https://www.nature.com/articles/s43588-023-00428-z>. Number: 4 Publisher: Nature Publishing Group.

Hannes Jónsson, Greg Mills, and Karsten W. Jacobsen. Nudged elastic band method for finding minimum energy paths of transitions. In *Classical and Quantum Dynamics in Condensed Phase Simulations*, pp. 385–404. WORLD SCIENTIFIC, June 1998. ISBN 978-981-02-3498-0. doi: 10.1142/9789812839664_0016. URL https://www.worldscientific.com/doi/abs/10.1142/9789812839664_0016.

Diederik P. Kingma and Jimmy Ba. Adam: A Method for Stochastic Optimization, January 2017. URL <http://arxiv.org/abs/1412.6980>. arXiv:1412.6980.

H. W. Kuhn. The Hungarian method for the assignment problem. *Naval Research Logistics Quarterly*, 2(1-2):83–97, 1955. ISSN 1931-9193. doi: 10.1002/nav.3800020109. URL <https://onlinelibrary.wiley.com/doi/abs/10.1002/nav.3800020109>. _eprint: <https://onlinelibrary.wiley.com/doi/pdf/10.1002/nav.3800020109>.

Alessandro Laio and Michele Parrinello. Escaping free-energy minima. *Proceedings of the National Academy of Sciences*, 99(20):12562–12566, October 2002. doi: 10.1073/pnas.202427399. URL <https://www.pnas.org/doi/10.1073/pnas.202427399>. Publisher: Proceedings of the National Academy of Sciences.

Gianmarco Lazzeri, Hendrik Jung, Peter G. Bolhuis, and Roberto Covino. Molecular free energies, rates, and mechanisms from data-efficient path sampling simulations, July 2023. URL <http://arxiv.org/abs/2307.11240>. arXiv:2307.11240.

Jungyoon Lee, Michael Plainer, Yuanqi Du, Lars Holdijk, Rob Brekelmans, Dominique Beaini, and Kirill Neklyudov. Scaling Deep Learning Solutions for Transition Path Sampling. April 2025. URL <https://openreview.net/forum?id=PTcJ6NLs14>.

Kresten Lindorff-Larsen, Stefano Piana, Kim Palmo, Paul Maragakis, John L Klepeis, Ron O Dror, and David E Shaw. Improved side-chain torsion potentials for the Amber ff99SB protein force field. *Proteins*, 78(8):1950–1958, June 2010. ISSN 0887-3585. doi: 10.1002/prot.22711. URL <https://www.ncbi.nlm.nih.gov/pmc/articles/PMC2970904/>.

Luca Maragliano, Alexander Fischer, Eric Vanden-Eijnden, and Giovanni Ciccotti. String method in collective variables: Minimum free energy paths and isocommittor surfaces. *The Journal of Chemical Physics*, 125(2):024106, July 2006. ISSN 0021-9606. doi: 10.1063/1.2212942. URL <https://doi.org/10.1063/1.2212942>.

Ben Mildenhall, Pratul P. Srinivasan, Matthew Tancik, Jonathan T. Barron, Ravi Ramamoorthi, and Ren Ng. NeRF: Representing Scenes as Neural Radiance Fields for View Synthesis, August 2020. URL <http://arxiv.org/abs/2003.08934>. arXiv:2003.08934 [cs].

Kirill Neklyudov, Rob Brekelmans, Daniel Severo, and Alireza Makhzani. Action Matching: Learning Stochastic Dynamics from Samples. In *Proceedings of the 40th International Conference on Machine Learning*, pp. 25858–25889. PMLR, July 2023. URL <https://proceedings.mlr.press/v202/neklyudov23a.html>. ISSN: 2640-3498.

Kirill Neklyudov, Rob Brekelmans, Alexander Tong, Lazar Atanackovic, Qiang Liu, and Alireza Makhzani. A Computational Framework for Solving Wasserstein Lagrangian Flows, July 2024. URL <http://arxiv.org/abs/2310.10649>. arXiv:2310.10649 [cs].

Eyal Neria, Stefan Fischer, and Martin Karplus. Simulation of activation free energies in molecular systems. *The Journal of Chemical Physics*, 105(5):1902–1921, August 1996. ISSN 0021-9606. doi: 10.1063/1.472061. URL <https://doi.org/10.1063/1.472061>.

Roberto Olander and Ron Elber. Yet another look at the steepest descent path. *Journal of Molecular Structure: THEOCHEM*, 398-399:63–71, June 1997. ISSN 0166-1280. doi: 10.1016/S0166-1280(97)00038-9. URL <https://www.sciencedirect.com/science/article/pii/S0166128097000389>.

L. Onsager and S. Machlup. Fluctuations and Irreversible Processes. *Physical Review*, 91(6):1505–1512, September 1953. doi: 10.1103/PhysRev.91.1505. URL <https://link.aps.org/doi/10.1103/PhysRev.91.1505>. Publisher: American Physical Society.

M. Petersen, G. Roig, and R. Covino. Teld: Trajectory-Level Langevin Dynamics for Versatile Constrained Sampling, December 2024. URL https://scholar.google.com/citations?view_op=view_citation&hl=en&user=yWSSx4wAAAAJ&citation_for_view=yWSSx4wAAAAJ:9yKSN-GCB0IC.

Magnus Petersen, Gemma Roig, and Roberto Covino. DynamicsDiffusion: Generating and Rare Event Sampling of Molecular Dynamic Trajectories Using Diffusion Models. October 2023. URL <https://openreview.net/forum?id=pwYCCq4xAF>.

Lawrence R. Pratt. A statistical method for identifying transition states in high dimensional problems. *The Journal of Chemical Physics*, 85(9):5045–5048, November 1986. ISSN 0021-9606. doi: 10.1063/1.451695. URL <https://doi.org/10.1063/1.451695>.

M. Raissi, P. Perdikaris, and G. E. Karniadakis. Physics-informed neural networks: A deep learning framework for solving forward and inverse problems involving nonlinear partial differential equations. *Journal of Computational Physics*, 378:686–707, February 2019. ISSN 0021-9991. doi: 10.1016/j.jcp.2018.10.045. URL <https://www.sciencedirect.com/science/article/pii/S0021999118307125>.

Sanjeev Raja, Martin Šípka, Michael Psenka, Tobias Kreiman, Michal Pavelka, and Aditi S. Krishnapriyan. Action-Minimization Meets Generative Modeling: Efficient Transition Path Sampling with the Onsager-Machlup Functional, April 2025. URL <http://arxiv.org/abs/2504.18506>. arXiv:2504.18506 [cs].

Kalyan Ramakrishnan, Lars L. Schaaf, Chen Lin, Guangrun Wang, and Philip Torr. Implicit Neural Representations for Chemical Reaction Paths, February 2025. URL <http://arxiv.org/abs/2502.15843>. arXiv:2502.15843 [cs].

Pratik Rathore, Weimu Lei, Zachary Frangella, Lu Lu, and Madeleine Udell. Challenges in Training PINNs: A Loss Landscape Perspective, June 2024. URL <http://arxiv.org/abs/2402.01868>. arXiv:2402.01868 [cs].

Weiqing Ren, Eric Vanden-Eijnden, Paul Maragakis, and Weinan E. Transition pathways in complex systems: Application of the finite-temperature string method to the alanine dipeptide. *The Journal of Chemical Physics*, 123(13):134109, October 2005. ISSN 0021-9606. doi: 10.1063/1.2013256.

David E. Shaw, Paul Maragakis, Kresten Lindorff-Larsen, Stefano Piana, Ron O. Dror, Michael P. Eastwood, Joseph A. Bank, John M. Jumper, John K. Salmon, Yibing Shan, and Willy Wriggers. Atomic-Level Characterization of the Structural Dynamics of Proteins. *Science*, 330(6002):341–346, October 2010. doi: 10.1126/science.1187409. URL <https://www.science.org/doi/full/10.1126/science.1187409>. Publisher: American Association for the Advancement of Science.

Daniel Sheppard, Rye Terrell, and Graeme Henkelman. Optimization methods for finding minimum energy paths. *The Journal of Chemical Physics*, 128(13):134106, April 2008. ISSN 0021-9606. doi: 10.1063/1.2841941. URL <https://doi.org/10.1063/1.2841941>.

Aditya N. Singh and David T. Limmer. Variational deep learning of equilibrium transition path ensembles. *The Journal of Chemical Physics*, 159(2):024124, July 2023. ISSN 0021-9606, 1089-7690. doi: 10.1063/5.0150278. URL <http://arxiv.org/abs/2302.14857>. arXiv:2302.14857 [physics].

Vincent Sitzmann, Julien N. P. Martel, Alexander W. Bergman, David B. Lindell, and Gordon Wetzstein. Implicit Neural Representations with Periodic Activation Functions, June 2020. URL <http://arxiv.org/abs/2006.09661>. arXiv:2006.09661 [cs].

G. M. Torrie and J. P. Valleau. Nonphysical sampling distributions in Monte Carlo free-energy estimation: Umbrella sampling. *Journal of Computational Physics*, 23(2):187–199, February 1977. ISSN 0021-9991. doi: 10.1016/0021-9991(77)90121-8. URL <https://www.sciencedirect.com/science/article/pii/0021999177901218>.

Alexander Ulitsky and Ron Elber. A new technique to calculate steepest descent paths in flexible polyatomic systems. *The Journal of Chemical Physics*, 92(2):1510–1511, January 1990. ISSN 0021-9606. doi: 10.1063/1.458112. URL <https://doi.org/10.1063/1.458112>.

Eric Vanden-Eijnden and Matthias Heymann. The geometric minimum action method for computing minimum energy paths. *The Journal of Chemical Physics*, 128(6):061103, February 2008. ISSN 0021-9606. doi: 10.1063/1.2833040. URL <https://doi.org/10.1063/1.2833040>.

Xinyan Wang, Jichen Li, Lan Yang, Feiyang Chen, Yingze Wang, Junhan Chang, Junmin Chen, Wei Feng, Linfeng Zhang, and Kuang Yu. DMFF: An Open-Source Automatic Differentiable Platform for Molecular Force Field Development and Molecular Dynamics Simulation. *Journal of Chemical Theory and Computation*, 19(17):5897–5909, September 2023. ISSN 1549-9618. doi: 10.1021/acs.jctc.2c01297. URL <https://doi.org/10.1021/acs.jctc.2c01297>. Publisher: American Chemical Society.

Jiawei Yan, Hugo Touchette, and Grant M. Rotskoff. Learning nonequilibrium control forces to characterize dynamical phase transitions. *Physical Review E*, 105(2):024115, February 2022. ISSN 2470-0045, 2470-0053. doi: 10.1103/PhysRevE.105.024115. URL <http://arxiv.org/abs/2107.03348>. arXiv:2107.03348 [cond-mat].

A TECHNICAL APPENDICES AND SUPPLEMENTARY MATERIAL

A.1 EXTENDED DERIVATION OF THE ENERGY-BASED LOSS FUNCTION

In this appendix, we provide a comprehensive derivation of our energy-based loss function for discovering minimum-energy paths (MEPs) between molecular configurations. The derivation proceeds in four main steps: (1) establishing the path probability density from overdamped Langevin dynamics, (2) reformulating this probability in terms of the Onsager-Machlup action functional, (3) simplifying this functional to a geometric line integral, and (4) developing a discretized approximation suitable for neural network optimization.

Our goal is to find the most probable transition path between two stable molecular configurations x_A and x_B . This path corresponds to the minimum-energy pathway through the potential energy landscape and represents the most likely mechanism of conformational change.

ASSUMPTIONS AND APPROXIMATIONS

The derivation relies on several key assumptions:

- The molecular system evolves according to overdamped Langevin dynamics, appropriate for high-friction biomolecular environments
- The path endpoints x_A and x_B are fixed and correspond to stable states
- The potential energy function $U(x)$ is differentiable everywhere along the path
- We can represent the path as a continuous, parameterized curve in configuration space with sufficient flexibility
- The path’s parameterization allows for effective length changes, permitting the path to adjust its stretching as needed to follow energy gradients optimally

We also make several important approximations during the derivation:

- We use a first-order Taylor expansion to relate energy differences to gradient magnitudes
- We introduce stochastic sampling to estimate the continuous energy integral
- For a MEP, the displacement tends to align either parallel or anti-parallel with the gradient direction (i.e., $\cos \theta_k \rightarrow \pm 1$ for path segments)
- We use the triangle inequality to establish an upper bound on the sum of absolute energy differences

While the last two approximations do not change the location of the global minimum, they do affect the optimization landscape before that minimum is reached.

A.1.1 FROM THE ONSAGER-MACHLUP ACTION TO A GEOMETRIC LINE INTEGRAL

We begin with a molecular system evolving under overdamped Langevin dynamics, a standard model for high-friction molecular motion:

$$\dot{x}(t) = -\nabla U(x(t)) + \sqrt{2}\eta(t) \quad (23)$$

where $x(t) \in \mathbb{R}^{3N}$ represents the molecular configuration, $U(x)$ is the potential energy function, and $\eta(t)$ is a Gaussian white noise with $\langle \eta_i(t)\eta_j(t') \rangle = \delta_{ij}\delta(t-t')$.

To derive the path probability, we discretize the time interval $[0, T]$ into N steps of duration Δt , approximating the dynamics as:

$$x_{i+1} = x_i - \Delta t \nabla U(x_i) + \sqrt{2\Delta t} \eta_i \quad (24)$$

where η_i are independent standard Gaussian random variables with zero mean and unit variance.

The conditional probability of transitioning from x_i to x_{i+1} follows a Gaussian distribution:

$$P(x_{i+1}|x_i) = \frac{1}{\sqrt{4\pi\Delta t}^d} \exp\left(-\frac{(x_{i+1} - x_i + \Delta t \nabla U(x_i))^2}{4\Delta t}\right) \quad (25)$$

$$\propto \exp\left(-\frac{(x_{i+1} - x_i + \Delta t \nabla U(x_i))^2}{4\Delta t}\right) \quad (26)$$

where d is the dimensionality of the system. The probability of the entire discretized path $\{x_0, x_1, \dots, x_N\}$ is given by the product of these conditional probabilities:

$$P(x_0, x_1, \dots, x_N) = P(x_0) \prod_{i=0}^{N-1} P(x_{i+1}|x_i) \quad (27)$$

$$\propto \prod_{i=0}^{N-1} \exp\left(-\frac{(x_{i+1} - x_i + \Delta t \nabla U(x_i))^2}{4\Delta t}\right) \quad (28)$$

$$= \exp\left(-\sum_{i=0}^{N-1} \frac{(x_{i+1} - x_i + \Delta t \nabla U(x_i))^2}{4\Delta t}\right) \quad (29)$$

Taking the limit as $\Delta t \rightarrow 0$ and $N \rightarrow \infty$ with $N\Delta t = T$ fixed, this sum approaches a path integral:

$$\lim_{\substack{\Delta t \rightarrow 0 \\ N\Delta t = T}} \sum_{i=0}^{N-1} \frac{(x_{i+1} - x_i + \Delta t \nabla U(x_i))^2}{4\Delta t} = \frac{1}{4} \int_0^T \left\| \dot{x}(t) + \nabla U(x(t)) \right\|^2 dt \quad (30)$$

Thus, the path probability can be written as:

$$\mathbb{P}[x(t)] \propto \exp\left(-\frac{1}{4} \int_0^T \left\| \dot{x}(t) + \nabla U(x(t)) \right\|^2 dt\right) \quad (31)$$

The exponent term is recognized as the Onsager-Machlup action functional:

$$S_{\text{OM}}[x] = \frac{1}{4} \int_0^T \left\| \dot{x}(t) + \nabla U(x(t)) \right\|^2 dt \quad (32)$$

This action functional penalizes paths that deviate from following the force $-\nabla U(x)$. Maximizing the probability of a transition path (subject to fixed endpoints $x(0) = x_A$ and $x(T) = x_B$) is equivalent to minimizing this action functional.

Expanding the integrand:

$$\left\| \dot{x}(t) + \nabla U(x(t)) \right\|^2 = \left\| \dot{x}(t) \right\|^2 + 2\dot{x}(t) \cdot \nabla U(x(t)) + \left\| \nabla U(x(t)) \right\|^2 \quad (33)$$

For paths with fixed endpoints $x(0) = x_A$ and $x(T) = x_B$, the cross-term integrates to a constant difference in potential energy:

$$\int_0^T \dot{x}(t) \cdot \nabla U(x(t)) dt = \int_0^T \frac{d}{dt} U(x(t)) dt = U(x_B) - U(x_A) \quad (34)$$

We can define a modified action functional that, when minimized, is equivalent to minimizing the original Onsager-Machlup functional for fixed endpoints:

$$\tilde{S}[x] = \int_0^T (\left\| \dot{x}(t) \right\|^2 + \left\| \nabla U(x(t)) \right\|^2) dt \quad (35)$$

By the Cauchy-Schwarz inequality:

$$\left\| \dot{x}(t) \right\|^2 + \left\| \nabla U(x(t)) \right\|^2 \geq 2\left\| \dot{x}(t) \right\| \left\| \nabla U(x(t)) \right\| \quad (36)$$

with equality when $\dot{x}(t)$ is parallel or anti-parallel to $\nabla U(x(t))$, with the direction determined by whether the path is ascending or descending the energy landscape. This is precisely the defining characteristic of the MEP - a path that follows the potential energy landscape's gradient while avoiding high-energy regions.

When this equality holds, our action simplifies to:

$$\tilde{S}[x] = \int_0^T 2\|\dot{x}(t)\|\|\nabla U(x(t))\|dt \quad (37)$$

The term $\|\dot{x}(t)\|dt$ represents the infinitesimal arc length element ds_{arc} along the path, allowing us to rewrite the action as a line integral:

$$S_{\text{geo}}[x] = 2 \int_{\varphi} \|\nabla U(x)\| ds_{\text{arc}} \quad (38)$$

where φ is the path in configuration space. This geometric form is independent of the path's parameterization and depends solely on the potential energy landscape.

A.1.2 DISCRETIZATION AND CONNECTION TO ENERGY DIFFERENCES

To compute this geometric action numerically, we introduce a progress coordinate $s \in [0, 1]$ and a mapping $\varphi_{\theta}(s)$ such that $\varphi_{\theta}(0) = x_A$ and $\varphi_{\theta}(1) = x_B$, where θ represents the network parameters. The relationship between the progress coordinate and arc length is:

$$ds_{\text{arc}} = \left\| \frac{d\varphi_{\theta}}{ds} \right\| ds \quad (39)$$

We discretize the path with L points, setting $s_k = \frac{k}{L-1}$ and $\varphi_k = \varphi_{\theta}(s_k)$ for $k = 0, 1, \dots, L-1$. The discretized geometric action becomes:

$$S_{\text{geo}}[\varphi_{\theta}] \approx 2 \sum_{k=0}^{L-2} \|\nabla U(\varphi_k)\| \cdot \|\Delta\varphi_k\| \quad (40)$$

where $\Delta\varphi_k = \varphi_{k+1} - \varphi_k$.

Using Taylor's theorem, we can relate energy differences to gradient magnitudes:

$$U(\varphi_{k+1}) - U(\varphi_k) = \nabla U(\varphi_k) \cdot \Delta\varphi_k + O(\|\Delta\varphi_k\|^2) \quad (41)$$

$$= \|\nabla U(\varphi_k)\| \|\Delta\varphi_k\| \cos \theta_k + O(\|\Delta\varphi_k\|^2) \quad (42)$$

where R_k is the remainder of the order $O(\|\Delta\varphi_k\|^2)$ and θ_k is the angle between the gradient and displacement vectors.

For a path following the minimum-energy trajectory, the gradient aligns with or against the path direction ($\cos \theta_k \rightarrow \pm 1$ as $\Delta s \rightarrow 0$, depending on whether the path is ascending or descending the energy landscape), giving at the minimum of the optimization:

$$|U(\varphi_{k+1}) - U(\varphi_k)| \approx \|\nabla U(\varphi_k)\| \cdot \|\Delta\varphi_k\| \quad (43)$$

This yields an approximation of the geometric action:

$$S_{\text{geo}}[\varphi_{\theta}] \approx 2 \sum_{k=0}^{L-2} |U(\varphi_{k+1}) - U(\varphi_k)| \quad (44)$$

This forms a surrogate objective with the same minimum as our original action.

A.1.3 ESTABLISHING THE ENERGY-BASED LOSS FUNCTION

We need to bound the sum of absolute energy differences to establish a direct connection to an energy-based loss function. Using the triangle inequality, for any two points and any constant c :

$$|U(\varphi_{k+1}) - U(\varphi_k)| \leq \frac{(U(\varphi_{k+1}) - c) + (U(\varphi_k) - c)}{2} = \frac{U(\varphi_{k+1}) + U(\varphi_k) - 2c}{2} \quad (45)$$

Choosing $c = \min_{s \in [0,1]} U(\varphi_\theta(s))$ to be the minimum energy along the entire path and summing over all segments:

$$\sum_{k=0}^{L-2} |U(\varphi_{k+1}) - U(\varphi_k)| \leq \sum_{k=0}^{L-2} \frac{U(\varphi_{k+1}) + U(\varphi_k) - 2c}{2} \quad (46)$$

$$= \frac{1}{2} \left(\sum_{k=0}^{L-2} U(\varphi_{k+1}) + \sum_{k=0}^{L-2} U(\varphi_k) - 2(L-1)c \right) \quad (47)$$

We can rewrite the first sum as $\sum_{k=1}^{L-1} U(\varphi_k)$ and the second as $\sum_{k=0}^{L-2} U(\varphi_k)$. Combining these terms:

$$\sum_{k=0}^{L-2} |U(\varphi_{k+1}) - U(\varphi_k)| \leq \frac{1}{2} \left(\sum_{k=1}^{L-1} U(\varphi_k) + \sum_{k=0}^{L-2} U(\varphi_k) - 2(L-1)c \right) \quad (48)$$

$$= \frac{1}{2} \left(\sum_{k=0}^{L-1} U(\varphi_k) - U(\varphi_0) + \sum_{k=0}^{L-1} U(\varphi_k) - U(\varphi_{L-1}) - 2(L-1)c \right) \quad (49)$$

$$= \sum_{k=0}^{L-1} U(\varphi_k) - \frac{U(\varphi_0) + U(\varphi_{L-1})}{2} - (L-1)c \quad (50)$$

Since c , $U(\varphi_0)$, and $U(\varphi_{L-1})$ are constants during optimization, minimizing $\sum_{k=0}^{L-1} U(\varphi_k)$ is equivalent to minimizing the upper bound on the geometric action. This provides the theoretical justification for our energy-based loss function.

A.1.4 NEURAL NETWORK IMPLEMENTATION

For practical optimization, we parametrize the path using a neural network $\varphi_\theta(s)$ with parameters θ . To implement our approach, we sample points along the path and minimize the energy at these sampled locations. This represents a transition from the theoretical derivation using discrete segments to a practical implementation using sampled points for more efficient optimization. We employ stochastic sampling of the progress coordinate to construct our loss function:

$$\mathcal{L}(\theta) = \frac{1}{B} \sum_{j=1}^B U(\varphi_\theta(s_j)) \quad (51)$$

where $s_j \sim \mathcal{U}[0, 1]$ are uniformly sampled progress coordinates and B is the batch size (the number of points sampled along the path during each optimization step).

This stochastic approach provides an unbiased estimator of the expected energy along the path:

$$\mathbb{E}_{s \sim \mathcal{U}[0,1]} [U(\varphi_\theta(s))] = \int_0^1 U(\varphi_\theta(s)) ds \quad (52)$$

By minimizing $\mathcal{L}(\theta)$ through gradient-based optimization, the neural network learns to represent low-energy pathways connecting the stable states, effectively discovering the MEP predicted by the Onsager-Machlup framework. The resulting path follows the potential energy landscape's gradient while avoiding high-energy regions, representing the most probable transition mechanism in the overdamped limit.

A.2 CONNECTION BETWEEN DOOB'S LAGRANGIAN AND MEP OPTIMIZATION

We elaborate on the theoretical connections between our energy-based optimization approach and the framework of Doob's h-transform for sampling transition paths (Du et al., 2024). This comparison is particularly relevant as both methods employ neural networks to represent molecular state transitions—either as a minimum-energy path in our case or the full transition path ensemble in theirs.

Notably, the parametrization of the mean trajectory in Du et al. resembles our MEP representation, differing primarily in our use of blending functions and spatial embeddings for the neural network component.

Doob’s Lagrangian formulation considers the following action functional:

$$S = \min_{q,v} \int_0^T dt \int dx q_{t|0,T}(x) \langle v_{t|0,T}(x), G_t v_{t|0,T}(x) \rangle \quad (53)$$

This functional quantifies the cost of controlling a stochastic process to achieve desired endpoint conditions, subject to the system’s energy landscape. Intuitively, it measures the amount of "effort"/action needed to steer the dynamics from starting state A to target state B, with smaller values indicating more probable transition paths.

In this formulation, $q_{t|0,T}(x)$ is the probability density at time t given boundary conditions, parameterized as a Gaussian $\mathcal{N}(x|\mu_{t|0,T}, \Sigma_{t|0,T})$, and $v_{t|0,T}(x)$ is the control vector field satisfying $v_{t|0,T}(x) = \frac{1}{2}(G_t)^{-1}(u_{t|0,T}(x) - b_t(x))$, with $b_t(x) = -\nabla V(x)$ representing the reference drift for overdamped dynamics.

This action functional describes a Wasserstein Lagrangian flow as formalized in (Neklyudov et al., 2023) and (Neklyudov et al., 2024). In this framework, one can learn stochastic dynamics from samples, thereby learning a process that defines a time-dependent density evolving from initial to final states.

The key difference with our PINN-MEP approach is that we minimize the action of a single deterministic path rather than a full distribution of paths. Mathematically, this corresponds to working with a single trajectory through configuration space rather than an ensemble of possible trajectories. This simplification is reflected in our loss function, which contains one fewer expectation than the full Doob’s Lagrangian.

A.2.1 COMPARISON WITH DOOB’S LAGRANGIAN METHOD

We provide a direct comparison between our PINN-MEP approach and the method of Du et al. in terms of computational efficiency, as evaluated by the number of force field/energy function calls, and the maximum energies observed in the paths, corresponding to the peak of the potential barrier. To provide a rigorous comparison, we conducted benchmarks using experimental conditions identical to those reported by Du et al. for alanine dipeptide: AMBER14 force field, 300K temperature. Table 1 presents these results alongside those reported in Du et al. (2024) and their recent follow-up work Lee et al. (2025). The only exception is that we do not evaluate trajectory probability, as the assumption of optimization over a non-physical path length makes the calculation of this quantity impossible.

PINN-MEP requires approximately 3261× fewer energy function evaluations (15.7K vs. 51.20M) compared to the Doob’s Lagrangian approach while achieving a 4.44 times lower maximum energy barrier. The lower number of required evaluations is likely due to the computation of the loss, which requires sampling their path $q_{t|0,T}$ over both T , as we do as well, but also the width of the path. Thus, the tradeoff of sacrificing full ensemble characterisation is expected to come with computational efficiency.

B COMPARISON WITH OTHER RELATED METHODS

While our primary benchmark comparison focuses on the Doob’s Lagrangian method due to similarity in task and system setup, examining how our approach relates to other methods for transition path discovery/MEP generation is also informative. Here we present results from two related approaches in the literature, though we emphasize that direct numerical comparisons should be treated with caution due to differences in force fields, optimization objectives, and units used.

Table 2 shows results from Ramakrishnan et al. (2025) comparing Nudged Elastic Band (NEB) with their Implicit Neural Representation (INR) approach for MEP discovery. Both our PINN-MEP approach and their INR method utilize lightweight, preexisting molecular dynamics force fields,

Table 1: Comparison of Doob’s Lagrangian and PINN-MEP approach on alanine dipeptide

Method	States	# Evaluations	Max Energy	MinMax Energy
MCMC variable length	CV	21.02M	740.70 ± 695.79	52.37
MCMC*	CV	1.29B	288.46 ± 128.31	60.52
MCMC variable length	relaxed	187.54M	412.65 ± 334.70	26.97
MCMC	relaxed	> 10B	N/A	N/A
MCMC variable length	exact	> 10B	N/A	N/A
MCMC	exact	> 10B	N/A	N/A
Doob’s Cartesian	exact	38.40M	726.40 ± 0.07	726.18
Doob’s Cartesian, 2 Mixtures	exact	51.20M	709.38 ± 162.37	513.72
Doob’s Cartesian, 5 Mixtures	exact	51.20M	541.26 ± 278.20	247.96
Doob’s Internal	exact	38.40M	-14.62 ± 0.02	-14.67
Doob’s Internal, 2 Mixtures	exact	51.20M	-15.38 ± 0.14	-15.54
Doob’s Internal, 5 Mixtures	exact	51.20M	-15.50 ± 0.31	-15.95
Doob’s Seq2Seq	exact	-	1505.6 ± 0.45	245.05 ± 0.02
w/ Temperature Annealing	exact	-	1583.18 ± 0.3	592.13 ± 0.26
w/ Interatomic Interpolation	exact	-	1601.57 ± 0.53	3.46 ± 0.03
MaxLL	exact	-	1532.45	615
w/ Temperature Annealing	exact	-	1599.03	233
w/ Interatomic Interpolation	exact	-	1545.32	619
PINN-MEP	exact	15700	-67.22 ± 3.55	-70.78

Table 2: Comparison between nudged elastic band (NEB) and implicit neural representation (INR) approaches for alanine dipeptide, adapted from Ramakrishnan et al. (2025). The table shows the best transition state (TS) energies achieved by each method after their complete optimization procedure, alongside the total number of force field evaluations required. Their neural-based INR approach significantly outperforms the traditional NEB method in both metrics.

Method	# Evaluations	Max Energy (eV)
NEB	8063	11.0014
INR	3046	0.4070

though we employ different such force fields. Their approach requires a more complex loss function that evaluates both energy and forces along with path parameterization and its gradient (path velocity), but needs fewer force field evaluations than our method. It is important to note that the "Max Energy" reported in Table 2 is measured in electron volts (eV) and appears to be adjusted for ground state energy reference, which makes direct energy comparisons with our method challenging. The difference in force fields used further complicates any direct energy value comparisons between methods.

In contrast, Table 3 presents results from Raja et al. (2025), who take a fundamentally different approach by re-purposing pre-trained generative models to perform sampling of transition paths. A key advantage of their method is that the generative model provides significantly better initial guesses for transition paths based on learned molecular distributions. Their approach requires evaluating both the pretrained model (as a surrogate force field) and its gradient for their loss function, which is more computationally intense due to the high number of parameters of the pretrained model as compared to a physics-derived force field.

These tables corroborate our findings in the Doob’s Lagrangian comparison: methods optimizing for a single MEP consistently require orders of magnitude fewer force field evaluations than approaches that characterize the full transition path ensemble.

Table 3: Computational efficiency comparison between different sampling methods for transition paths on alanine dipeptide, adapted from Raja et al. (2025). The table compares traditional methods with an Onsager-Machlup (OM) optimization approach that uses a pre-trained diffusion model as a surrogate for molecular force fields. The “CVs” column indicates whether collective variables were required (a potential limitation). The dramatic reduction in both force field evaluations and runtime demonstrates the computational advantage of neural network-based approaches for transition path discovery.

Method	CVs	# Evaluations	Runtime / Path
MCMC (Two-Way Shooting)	No	$\geq 1B$	≥ 100 hours
Metadynamics	Yes	1M	10 hours
OM Opt. (Diffusion Model)	No	10K	50 min

B.1 ABLATION STUDIES

This section presents a series of ablation studies examining the impact of various components of our PINN-MEP approach. These experiments help validate our design choices and provide insights into the importance of different architectural and training elements. We conduct these ablation studies on the AIB9 system because Alanine dipeptide, as a benchmark system, is too simple to provide meaningful insights into the performance of our method. For each ablation study, we report the lowest maximum energy of the path among all training runs, the mean and standard deviation of the energy, and the mean number of iterations to reach the lowest maximum energy. We run each setting in the ablations 15 times for a maximum of 25,000 iterations. We use a batch size of 1, where each batch contains 32 values of the progress coordinate s for most cases. The exception is when we evaluate the chain-of-states-like regularization, which minimizes the difference between network outputs for adjacent values of s ; in this case, the effective batch size is 32, since there are no interactions between different network outputs otherwise.

Due to the nature of physical force fields, slight deviations in the path can lead to large changes in energy, leading to similar settings having very different energies. This can limit the ability to compare the performance of different settings. However, we find that the results are still directionally informative.

B.1.1 GENERAL SETTINGS FOR ABLATION STUDIES

All ablation studies are conducted using the following base configuration, with each study varying only specific parameters while keeping all others fixed:

Molecular System Parameters:

- Molecular system: AIB9 peptide with 129 atoms
- Force field: AMBER ff15ipq-m for protein mimetics
- Cutoff method: No cutoff applied
- Simulation box size: 10.0 nm
- Neighbor list cutoff distance: 4.0 nm

Training Configuration:

- Number of iterations: 25,000 per run
- Number of independent runs: 15 per parameter setting
- Evaluation frequency: Every 100 training steps
- Optimizer: Adam with optax default parameters
- Learning rate: 1×10^{-5}

Path Sampling Parameters:

- Batch size: 1
- Frames per batch: 32 points sampled along the progress coordinate s
- Spring constant: $k = 0$ (no chain-of-states regularization)
- Interpolation method: Cubic Hermite for blending functions

Network Architecture (Base Configuration):

- Network depth: 6 hidden layers
- Width factor: 4 (network width scales as $4 \times$ number of atoms)
- Embedding dimension: Automatically set to width factor \times number of atoms
- Time embedding: Sinusoidal with maximum period of 10^6
- Activation function: ReLU throughout the network
- Weight initialization: Glorot uniform for hidden layers, zero initialization for final layer
- Bias initialization: Default for hidden layers, zero initialization for final layer

B.1.2 EMBEDDING STRATEGY

We compared sinusoidal time embeddings with different maximum periods against simple linear projections of the progress coordinate. Table 4 shows that linear embedding (None) performed best, achieving the lowest mean energy, though sinusoidal embeddings with period 10^6 also achieved competitive results. We find these results at odds with the need for sinusoidal embeddings in the larger BPTI system. Perhaps the AIB9 system, which is characterized by one large general conformational rearrangement primarily driven by main-chain dihedral angles, does not need the high frequency features that sinusoidal embeddings provide, but which might be essential for other systems, due to the well-known bias of MLPs toward modeling low frequencies in data.

Table 4: Impact of embedding strategy on MEP generation

Embedding	Max Period	MeanMax Energy ($\pm \sigma$)	MinMax Energy	Mean Iterations
Linear (None)	—	591.35 ± 963.72	-337.36	200873
Sinusoidal	10^6	1326.13 ± 2339.35	-337.36	210907
Sinusoidal	10^4	1528.18 ± 2429.05	-129.90	226290
Sinusoidal	10^3	1888.66 ± 3604.47	-337.36	187493
Sinusoidal	10^2	2453.53 ± 3507.47	-337.36	217053

B.1.3 SPRING REGULARIZATION

We tested the effect of chain-of-states-like spring constant regularization, as shown in Table 5. Interestingly, we found that small amounts of spring regularization ($k = 10^{-5}$ or $k = 10^{-4}$) provided the best results, with $k = 10^{-5}$ achieving the lowest mean energy overall. This suggests that a minimal amount of explicit path continuity enforcement can be beneficial when combined with our neural representation, though this is not a strict requirement for the method to work. However, adding a spring constant reintroduces intra-batch dependencies, which means that batch sizes should be of a minimum size for this approach to work effectively. With low batch sizes, this could lead to the corner cutting effects commonly observed in traditional chain-of-states methods, which might make scaling the addition of spring regularization difficult for larger systems. Since we are able to reach the same minimum energy without spring regularization, we recommend against its use, especially when scaling to larger systems where lower batch sizes are preferred.

B.1.4 NETWORK ARCHITECTURE

We investigated the effect of network depth and width on transition path quality. Table 6 shows that an 8-layer network with a width factor of 4 achieved the best mean energy performance, followed closely by a 6-layer network with width factor 6.

Table 5: Impact of spring constant regularization

Spring Constant k	MeanMax Energy ($\pm\sigma$)	MinMax Energy	Mean Iterations
10^{-5}	-178.22 ± 260.09	-337.36	153533
10^{-4}	-155.41 ± 286.63	-337.36	101600
10^{-3}	803.61 ± 586.95	205.74	159033
0.0	1460.41 ± 2486.05	-337.36	209133
10^{-2}	10528.4 ± 7394.89	5065.46	155400
10^{-1}	48639.7 ± 12111.7	33143.6	107267

Table 6: Network architecture ablation results

Depth	Width Factor	MeanMax Energy ($\pm\sigma$)	MinMax Energy	Mean Iterations
8	4	25.02 ± 467.23	-337.36	159333
6	6	72.42 ± 458.72	-337.36	210267
8	6	165.91 ± 1021.79	-337.36	219433
8	2	1434.97 ± 3206.06	-337.36	178167
6	4	1460.34 ± 2486.07	-337.36	209067
6	2	3621.8 ± 3198.25	217.83	231200
4	6	4242.74 ± 3568.51	140.81	231967
4	4	5130.75 ± 5758.01	-328.49	228133
4	2	16200.5 ± 8032.18	159.21	210367

B.1.5 INTERPOLATION TYPE

We examined different interpolation methods for the blending functions that combine the neural network output with the endpoint constraints. Table 7 compares linear, cosine, quintic, and cubic Hermite interpolation. Cosine interpolation performed best in terms of mean energy, though all methods were able to achieve the minimum energy of -337.36 in at least one run, except for quintic. The cubic Hermite interpolation showed higher variance in results.

The specific formulas for each interpolation type are as follows:

Linear interpolation:

$$h_0(t) = 1 - t \quad (54)$$

$$h_1(t) = t \quad (55)$$

$$b(t) = t(1 - t) \quad (56)$$

Cubic Hermite interpolation:

$$h_0(t) = (1 - t)^2(1 + 2t) \quad (57)$$

$$h_1(t) = t^2(3 - 2t) \quad (58)$$

$$b(t) = 4t(1 - t) \quad (59)$$

Quintic interpolation:

$$h_0(t) = 1 - t^3(6t^2 - 15t + 10) \quad (60)$$

$$h_1(t) = t^3(6t^2 - 15t + 10) \quad (61)$$

$$b(t) = 16t^2(1 - t)^2 \quad (62)$$

Cosine interpolation:

$$h_0(t) = \frac{1 + \cos(\pi t)}{2} \quad (63)$$

$$h_1(t) = \frac{1 - \cos(\pi t)}{2} \quad (64)$$

$$b(t) = \sin(\pi t) \quad (65)$$

where $h_0(t)$ and $h_1(t)$ are the basis functions that ensure endpoint constraints $\varphi_\theta(0) = x_A$ and $\varphi_\theta(1) = x_B$, and $b(t)$ is the blending function that controls the neural network’s contribution along the path.

Table 7: Impact of interpolation type on MEP generation

Interpolation Type	MeanMax Energy ($\pm\sigma$)	MinMax Energy	Mean Iterations
Cosine	442.51 ± 769.51	-337.36	198720
Linear	602.61 ± 1057.13	-337.36	219147
Quintic	967.16 ± 1288.57	-281.14	210227
Cubic Hermite	1325.49 ± 2339.75	-337.36	212807

B.1.6 AIB9 NETWORK ARCHITECTURE

Below are the main details of the AIB9 MEP training runs, as shown in the main paper.

- **Model type:** Transition MLP with sinusoidal time embedding
- **Network depth:** 6 hidden layers
- **Network width:** $4 \times$ width factor (scaled relative to the number of atoms)
- **Time embedding:** Sinusoidal position encoding with maximum period of 1,000,000
- **Activation function:** ReLU

B.1.7 TRAINING PARAMETERS

- **Optimizer:** Adam
- **Learning rate:** 1×10^{-5}
- **Batch size:** 4
- **Frames per batch:** 32
- **Spring constant (k):** 0.0
- **Interpolation method:** Linear

All other parameters are identical to the base settings listed in the ablations section B.1.1.

B.2 BPTI MODELING AND COMPUTATIONAL DETAILS

B.2.1 SYSTEM PREPARATION

As reference conformations, we used the structures from the D.E. Shaw Research BPTI simulation of BPTI (Shaw et al., 2010). The initial and final states for our MEP optimization were selected as the second snapshot (index 1) and the second-to-last snapshot (index -2) from the provided reference structures, as they were the most separated in the CVs determined in the original study, named the backbone RMSD and the disulfide torsion angle.

B.2.2 EXPLICIT SOLVENT SHELL CONSTRUCTION

For the BPTI system, we developed a sophisticated approach to handle explicit water molecules efficiently:

- **Initial water box generation:** Both start and end configurations were solvated with TIP3P water molecules using a padding distance of 2.0 nm and energy minimized for 15,000 steps.
- **Water shell extraction:** Rather than using the entire water box, we extracted spherical shells of water molecules within a 1.4 nm radius of any protein atom for both the start and end configurations. This significantly reduced the system size while maintaining the crucial first hydration shell.

- **Radius optimization:** We employed a binary search algorithm to determine optimal shell radii that would capture an identical number of water molecules in both start and end configurations, ensuring consistent system sizes throughout the transition.
- **Water molecule matching:** We applied the Hungarian algorithm to optimally pair water molecules between the start and end states based on spatial proximity, minimizing the overall displacement of water molecules during the transition, which ensures that the initial guess for the MEP does not have very large energies stemming from overlapping molecules.

B.2.3 HYBRID NEURAL NETWORK ARCHITECTURE

For the BPTI system with explicit solvent, we developed a specialized hybrid transition model to handle the larger system size efficiently:

- **Protein representation:** Neural network with 6 layers, a width factor of 4, and sinusoidal time embedding for the protein atoms (58 residues, 892 atoms)
- **Water representation:** Parameterized spline interpolation between matched water molecules
- **Control points:** 7 control points for the spline interpolation
- **Water weight:** 0.1 (relative weight of water molecule contributions to the loss)
- **Clamp threshold:** 1×10^{-4} (minimum/maximum energy clipping threshold)

B.2.4 TRAINING PARAMETERS

The BPTI MEP was optimized using the following training parameters:

- **Optimizer:** Adam
- **Learning rate:** 1×10^{-4}
- **Batch size:** 1
- **Frames per batch:** 16
- **Total iterations:** 30,000

All other parameters are identical to the base settings listed in the ablations section B.1.1.

B.2.5 HANDLING HIGH-ENERGY SPIKES DURING TRAINING

Physical force fields present unique optimization challenges due to occasional extreme energy spikes when atoms approach one another too closely. To address this, we implemented adaptive gradient clipping in our training procedure:

$$\text{clipped_grads} = \text{clip}(\nabla_{\theta} \mathcal{L}(\theta), \gamma) \quad (66)$$

where γ is a clipping threshold (set to 1×10^{-4} in our experiments). We specifically use adaptive gradient clipping rather than a fixed threshold because our hybrid architecture contains two fundamentally different parameter types: neural network weights for protein coordinates and spline control points for water molecules. The adaptive nature of the clipping automatically adjusts to the appropriate scale for each parameter type.

Additionally, we apply different scaling factors to these parameter groups:

$$\nabla_{\theta_{\text{water}}} \mathcal{L}(\theta) \leftarrow \alpha \cdot \nabla_{\theta_{\text{water}}} \mathcal{L}(\theta) \quad (67)$$

with $\alpha = 0.1$ for water-related parameters. This differential treatment further balances the influence of each component during optimization. While this approach does not completely eliminate training instabilities, we find it sufficient for most protein systems when combined with careful initialization and learning rate scheduling.

B.2.6 FORCE FIELD PARAMETERS

We used the following force field parameters to match the D.E. Shaw simulation conditions:

- **Protein force field:** AMBER99sb-ILDN (amber99sbildn.xml)
- **Water force field:** TIP3P (tip3p.xml)

B.2.7 COMPUTATIONAL PERFORMANCE

For the BPTI system with explicit solvent (approximately 8,300 atoms total):

- **Training time:** Approximately 7 to 15 minutes on a single NVIDIA A6000 GPU
- **Force field evaluations:** Approximately 480,000 evaluations (30,000 iterations x 16 frames per batch)
- **Trajectory generation:** 64 frames for the final MEP visualization and analysis

This computational effort is approximately six orders of magnitude less, in node-hours, than the original D.E. Shaw Research simulation on their specialized Anton supercomputer, which required approximately 1.3 million node-hours to generate the 1.03 millisecond trajectory capturing the same conformational changes.

B.2.8 COMPUTATIONAL RESOURCES

All experiments reported in this paper were conducted on a single NVIDIA A6000 GPU with 48GB of memory. Additional computational resources were used during the development phase of this project for hyperparameter tuning across network architectures and optimization parameters.